Quantification of uncertainty in 3-D seismic interpretation: implications for deterministic and stochastic geomodelling and machine learning

Alexander Schaaf[1] and Clare E. Bond[1]

[1]Geology and Petroleum Geology, School of Geosciences, University of Aberdeen, AB24 3UE, UK

Correspondence: a.schaaf@abdn.ac.uk

Abstract. In recent years uncertainty has been widely recognized in geosciences, leading to an increased need for its quantification. Predicting the subsurface is an especially uncertain effort, as our information either comes from spatially highly limited direct (1-D boreholes) or indirect 2-D and 3-D sources (e.g. seismic). And while uncertainty in seismic interpretation has been explored in 2-D, we currently lack both qualitatitive and quantitative understanding of how interpretational uncertainties of 3-D datasets are distributed. In this work we analyze 78 seismic interpretations done by final year undergraduate (BSc) students of a 3-D seismic dataset from the Gullfaks field located in the northern North Sea. The students used Petrel to interpret multiple (interlinked) faults and to pick the Base Cretaceous Unconformity and Top Ness horizon (part of the Mid-Jurassic Brent Group). We have developed open-source Python tools to explore and visualize the spatial uncertainty of the students fault stick interpretations, the subsequent variation in fault plane orientation and the uncertainty in fault network topology. The Top Ness horizon picks were used to analyze fault offset variations across the dataset and interpretations, with implications for fault throw. We investigate how this interpretational uncertainty interlinks with seismic data quality and the possible use of seismic data quality attributes as a proxy for interpretational uncertainty. Our work provides a first quantification of fault and horizon uncertainties in 3-D seismic interpretation, providing valuable insights into the influence of seismic image quality on 3-D interpretation, with implications for deterministic and stochastic geomodelling and machine learning.

1 Introduction

Geosciences, and geology in particular, are concerned with integrating various sources of data, often of limited, sparse and indirect nature, into scientific models. The use of limited data combined with our limited knowledge of the highly complex earth system, invariable infuses any model with uncertainty. Especially as geology inherently relies heavily on interpreted data that often requires reasoning about processes that occur over geological time scales (Frodeman, 1995), which further increase the space of uncertainty.

The interpretation of 3-D seismic data is an integral part of constructing structural geomodels of the subsurface and plays a major role in the energy industry. Due to the indirect, noisy and non-unique nature of seismic data processing into images, interpretation is inherently uncertain. Previous work has shown that significant conceptual uncertainties and biases are encountered during the interpretation process of 2-D seismic lines (Bond et al., 2007, 2011; Macrae, 2013; Bond, 2015; Alcalde et al., 2017a, c), as well as the impact of seismic image quality on the interpretation (Alcalde et al., 2017b). But subsurface structures are naturally three-dimensional and the use of 3-D seismic data is ubiquitous in industry (Biondi, 2006)—which raises the need to further our understanding of the distribution of interpretational uncertainties in 3-D space. Additionally, the process of interpretation between seismic lines and cubes is fundamentally different, and thus might lead to conceptually different uncertainties to be dominant (e.g. the need to connect fault evidence between seismic lines introduces significant uncertainty in widely spaced 2-D interpretation compared to fault interpretation in seismic cubes; see Freeman et al., 1990).

In this work we investigate the scope of uncertainties in 3-D seismic interpretation. We qualitatively and quantitatively analyze interpretations of 78 final year undergraduate students (BSc) conducted on a 3-D seismic cube of the Gullfaks field. The dataset depicts a domino system of fault blocks with a comparatively simple structural style, but the seismic dataset comes with high amounts of noise throughout, which inhibits straight-forward interpretation of the major faults and horizons and limits use of structural seismic attributes. We analyze the spatial variation in fault stick interpretations and the subsequent uncertainty in fault orientation. Horizon interpretations are analyzed and combined with fault interpretations for a description of fault throw uncertainty. Additionally, we investigate the differences in fault network topology in the interpretation ensemble to better estimate the uncertainty of interpreting fault networks in 3-D seismic data. We use the interpretation of Fossen and Hesthammer (1998) as a reference expert example (in the sense of Macrae et al., 2016) for comparison with the student interpretations. We integrate our findings of interpretation uncertainties with its relation to seismic data quality and discuss the implications for both deterministic and stochastic geomodelling, as well as machine learning applied to seismic interpretation.

2 Materials and Methods

2.1 Gullfaks geology and seismic data

We give here a brief overview over the regional and structural geology of the study area; a more in-depth description of the structural geology of the Gullfaks Field can be found in Fossen and Hesthammer (1998).

The Gullfaks Field is a subset of the NNE-SSW-trending, $10 - 25$ km wide Gullfaks fault block, located in the western part of the Viking Graben within the North Sea (see Figure 1a). The Gullfaks field's reservoir units reach from the late Triassic Hegre Group, over the Early Jurassic Statfjord Formation, Dunlin Group up to the Brent Group (Hesthammer and Fossen, 1997). The reservoir units are separated from the Upper Cretaceous sediments above by the Base Cretaceous unconformity (Fossen and Hesthammer, 1998). The field consists of three structurally distinct subsets: a domino system in the western part, an accommodation zone and a Horst complex towards the east (see Figure 1c). Our study focuses on the major faults F1 - F3 and the fault blocks A - E depicted in Figure 1b, which are part of the western domino system. Note that Fault 1 and 2 merge in the northern half and at the bottom of the domain and that Fault 2 splits into two smaller faults F2a and F2b.
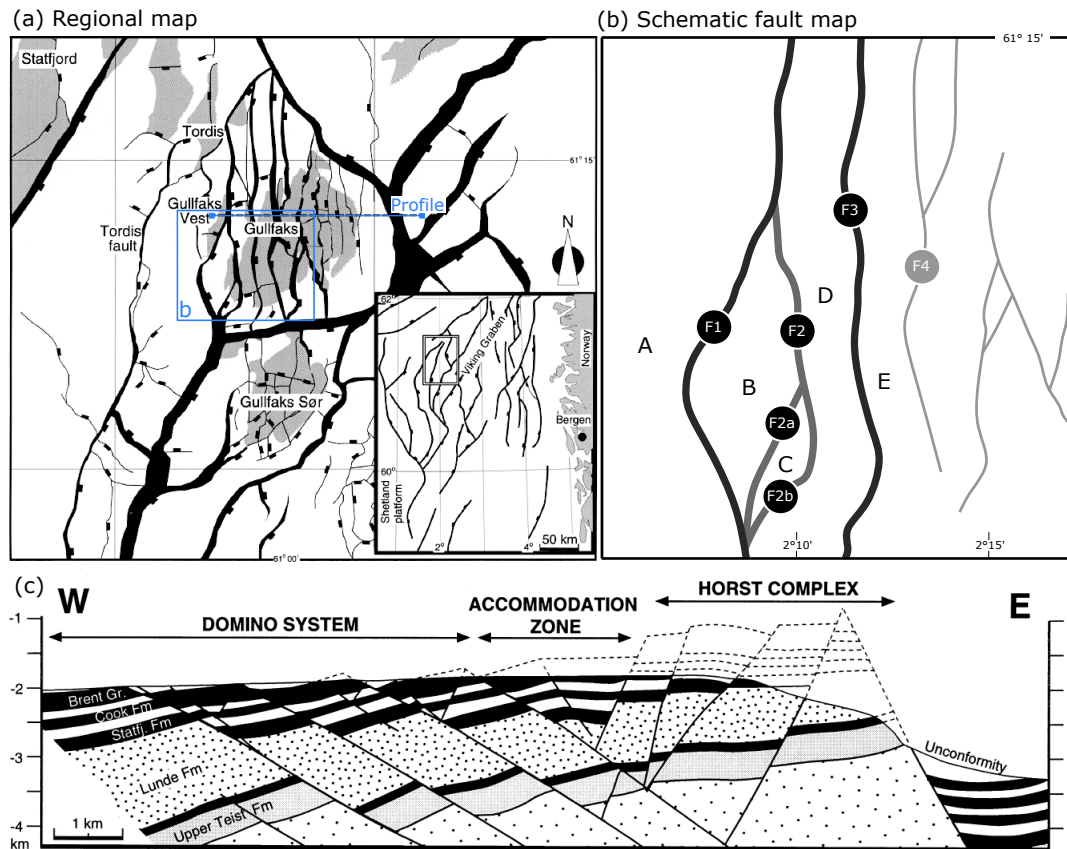
Figure 1. (a) Regional overview of the Gullfaks area located in the North Sea, showing the location of the Gullfaks oil field; (b) Fault map of the Statfjord formation, showing the main faults of the Gullfaks field and their labeling; (c) Cross-section across the Gullfaks field, depicting the three distinct structural subsets, major faults and stratigraphy (modified from Fossen and Hesthammer, 1998).

2.2 Interpretation dataset

The analyzed interpretations were produced as part of the Surface and Subsurface Digital Imaging course within the undergraduate program Geology and Petroleum Geology at the University of Aberdeen. The fourth year undergraduate (BSc) students loaded the seismic data into Petrel together with 14 wells, while ensuring proper georeferencing. The following interpretation

5 process focused on first interpreting the Top Cretaceous horizon with initial support by the lecturing staff. Afterwards the students started to independently interpret the Base Cretaceous Unconformity (BCU) and Top Ness horizon (which is part of the Brent group) around well locations, followed by connecting the horizon interpretation in-between wells using mainly guided auto-tracking, as well as occasional seeded tracking and manual interpretation. Afterwards fault interpretations were conducted of major faults. The students then interpolated gridded surfaces from the horizon interpretations using Petrel's *Make Surface*

10 function. Polygons were created based on fault locations to create a Top Ness surface subdivided into the fault blocks.
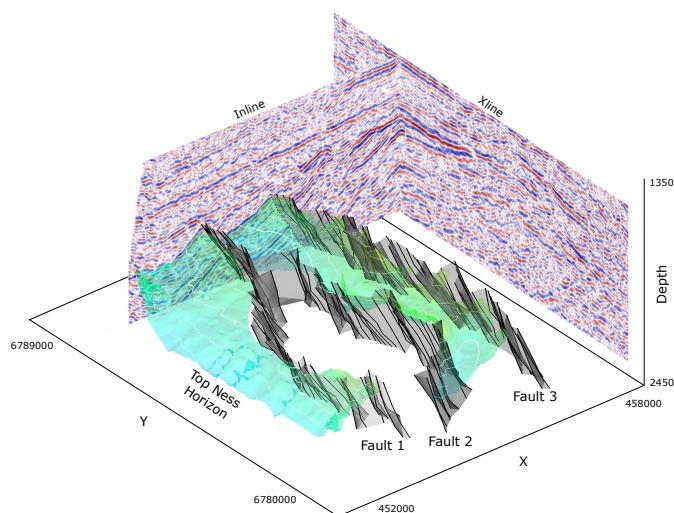
Figure 2. Example interpretation from a single student, showing the three major faults considered in our study as well as part of the Top Ness horizon interpretation. BCU and additional faults are hidden for better visualization of the key elements.

For our study we collated the interpretation data from the students Petrel projects into a joint project, where interpretations were sorted and labeled. Of a total of 90 student interpretations, we used 78 in our study, as the other 12 either lacked relevant interpretations or were corrupted Petrel project files. Interpreted Top Ness horizon surfaces and fault sticks where then exported systematically to allow for automated data processing and analysis. An example student interpretation is shown in Fig. 2, containing the three major faults considered, as well as the Top Ness horizon in two of the fault blocks A and D defined in Fig. 1b.

2.3 Data analysis

To process and analyze the large amount of interpretation data, the exported Petrel surfaces and fault sticks were wrangled using custom Python functionality and labeled in an open tabular data format. The result is a set of 4460878 data points, belonging to 78 student interpretations, with 228 unique faults considered, which consist of a total 10052 individual fault sticks. For data processing and analysis we made heavy use of the open-source Python packages *pandas*, *SciPy* and *NumPy* (McKinney, 2011; Jones et al., 2001; Oliphant, 2006).

For the purpose of visualization and statistical analysis of the fault interpretations across the collective interpretations, the domain was discretized into regular bins ($nx = 60$, $ny = 60$, $nz = 24$). In the following analysis we present 2-D and slices of 3-D histograms of fault interpretations, showing interpretation density and frequency across the domain. Fault orientations for individual faults were computed by fitting a plane (using singular-value decomposition) to all fault stick points of a single interpretation over all grid cells (collapsed along the x-axis). This makes the analysis less dependant on the fault stick interpretation density, which varies extensively in-between students. The resulting normal vector can be converted into strike and dip values.

For visualization the fault orientation data was subdivided into three regular bins oriented E-W across the structures. The fault throw analysis is based on the Top Ness horizon and is computed individually at each interpreted fault stick for each fault and each interpretation. The nearest data points on both the hanging and foot wall of the Ness horizon fault blocks were selected as seeds. From these seeds the surface data approximately orthogonal to strike was used within a strike-parallel window of three grid cells. A relative gradient filter was then used to exclude points with gradients to their nearest neighbors outside of the inner-quartile-range (IQR) of the selected subset. The resulting data is fitted with a linear regression for each fault block and the intersection with the fault stick used to calculate fault throw. For the assessment of seismic reflector strength an RMS Amplitude (RMSA) seismic attribute was calculated using Petrel. RMS Amplitude represents the square root of the arithmetic mean of squared amplitude values across a specified seismic trace window.

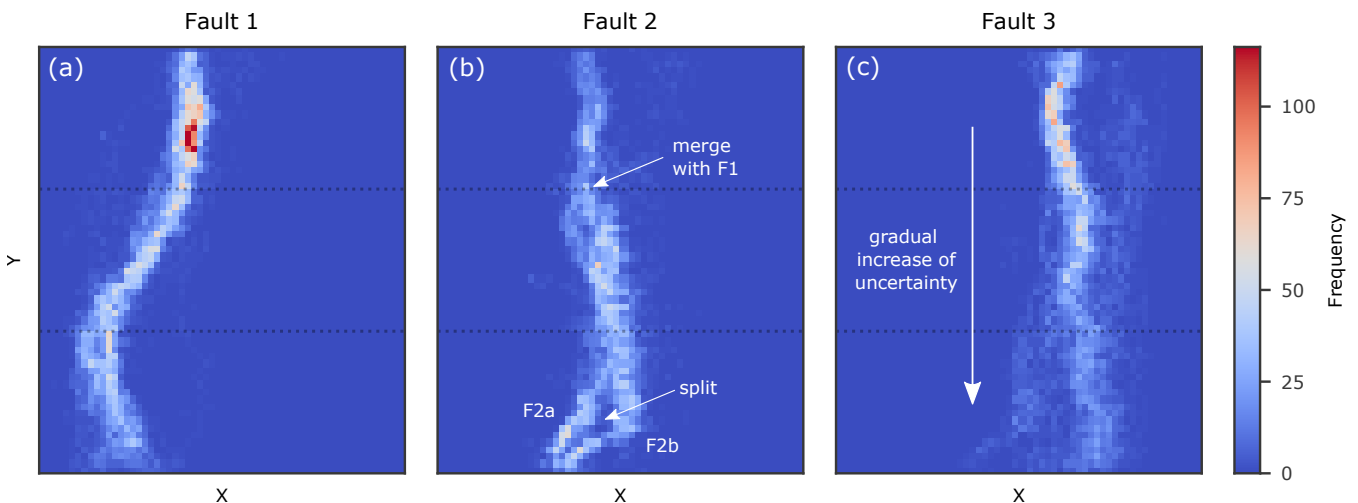## 3 Results

3.1 Uncertainty in fault interpretation

Figure 3. 2D Histograms for the three Faults 1 (a), 2 (b) and 3 (c) for depth slice at $2\ km\ \pm\ 0.1$. Horizontal lines separate the three bins used for plotting subsets of orientation data in Fig. 4.

Figure 3 shows 2-D histograms for the three major faults taken into consideration within this study. The histograms cover the entire extent of the seismic cube, with the frequency of fault stick points counted per bin in a depth slice at $2\ km\ \pm\ 0.1$. Fault 1 shows a sigmoidal shape in the N-S direction of the seismic depth slice (see Fig. 3a), with high frequency densities in the northern part and lower intensities found in the southern part. Plotting all fault plane orientations within a single stereonet reveals three distinct clusters of planes (Fig. 4a), which when separated into three equal bins along the N-S axis correspond to the components of the sigmoidal fault shape (Fig. 4b-d). Interpretations of Fault 2 show a split into two sub-faults F2a and F2b in the southern part (see Fig. 3b), as also interpreted by Fossen and Hesthammer (1998, see Fig. 1). The spatial uncertainty

of the fault interpretations appears slightly lower in the northern part of the seismic slice, but also shows evidence of a small separated fault block in the central part of the fault. The interpretations of Fault 3 show a strong increase in spread towards the southern part of the seismic slice (Fig. 3c). The same trend of increasing uncertainty can be observed in the fault plane orientation (Fig. 4j-l). Additionally, the histogram shows the occasional interpretation of the fault branching towards Fault 2(b), towards the West, and towards Fault 4 to the East (see Fig. 1b).
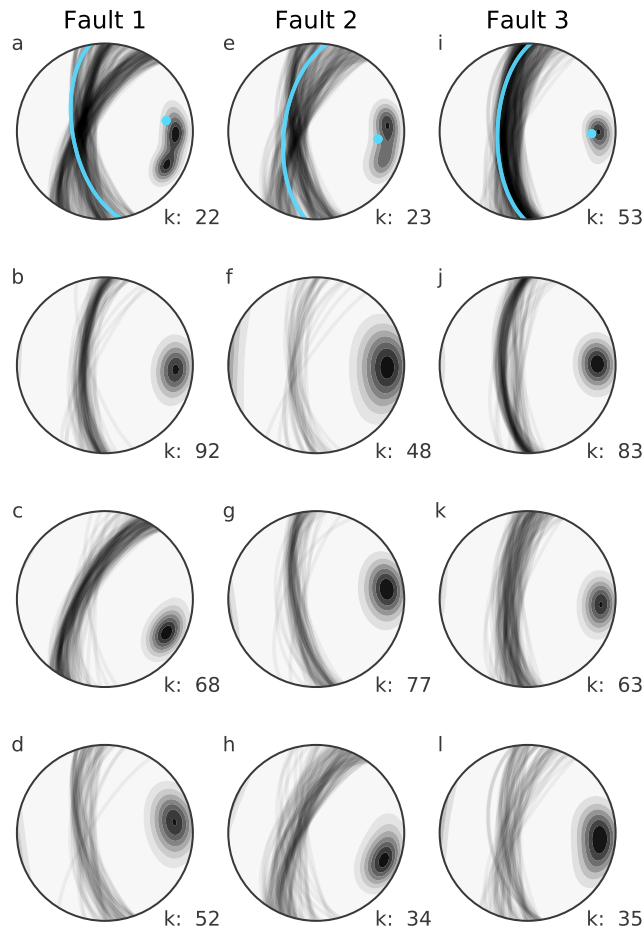

Figure 4. Stereonet plots of Faults 1-3 (columns), with all fault strike orientations along the fault length plotted combined in the first row (a, e, i). To discriminate changing trends in actual fault orientation from interpretation uncertainty rows two to four plot data from bins shown in Fig. 3, from the northern bin (c, g, k), middle (d, g, l) and south (e, h, m). Blue planes and poles in top row (a, e, i) show Bingham analysis mean pole from Fossen and Hesthammer (1998) for reference.

Figure 4 plots fault plane orientations calculated from students fault stick interpretations. Fault 1 shows three distinct clusters of orientations (Fig. 4a), which can be separated by subdividing the study domain into three equal bins along the N-S axis.

Fault 1 shows a striking decrease in k-values (a measure of tightness of the orientation clusters) from North to South (92, 68, 52). The pattern does not hold true for Fault 2, which shows low k-values both in the North and South. Fault 3 shows similar behaviour to Fault 1, with a strong increase in dispersion from North to South (83, 63, 35).
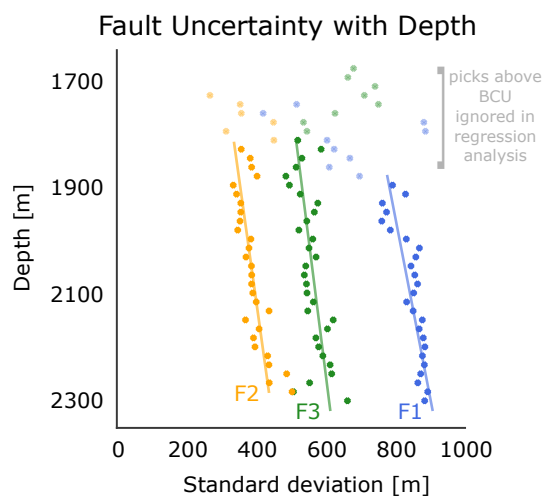

Figure 5. Scatter plot of mean (collapsed y-axis) standard deviation along x-axis of mean fault surfaces for Fault 1, 2 and 3. Chaotic patterns of uncertainty at shallow depths (faded data points) are likely due to sporadic numbers of interpretations, as students often stopped interpreting the faults before reaching the Base Cretaceous unconformity (BCU). Overall, uncertainty of fault interpretations is increasing linearly with depth (linear regression only takes into account interpretations below the BCU, R-values for Fault 1, 2 and 3 respectively: 0.75, 0.85 and 0.61).

Overall the observed uncertainty (standard deviation) of the fault plane along the W-E axis appears to be increasing linearly
5 with depth for all three faults (Fig. 5). Note that the overall mean standard deviations between the faults vary greatly: 791, 384 and 575 m for Faults 1, 2 and 3, respectively. The extremely high variation of standard deviations seen in the upper part of Fig. 5 (faded data points) is due to a few students extending their fault interpretations above the Base Cretaceous unconformity (BCU), making the data points at that depth statistically unreliable due to low sample numbers and geologically questionable. Any fault stick interpretations above the unconformity were thus excluded from the least-squares linear regression (R-values
10 for Fault 1, 2 and 3: 0.75, 0.85 and 0.61).

The ensemble of interpretations show 11 different fault network (FN) topologies (see Fig. 6a). Five modes of FN topology make up the bulk of fault network topologies, while all others occur with a probability of less than 0.05 each. The sketches in Fig. 6b represent these five most likely FNs (Fault 3 is omitted for brevity, as it was interpreted by all students in a similar fashion, and only a single student connected Fault 2 with Fault 3). Note that the most probable FN (Fig. 6b, A) is different
15 from the reference expert FN interpretation of Fossen and Hesthammer (1998), which corresponds to either the second or fourth most common FN interpretations (Fig. 6b, B and D). The major source of uncertainty in this specific FN appears to be
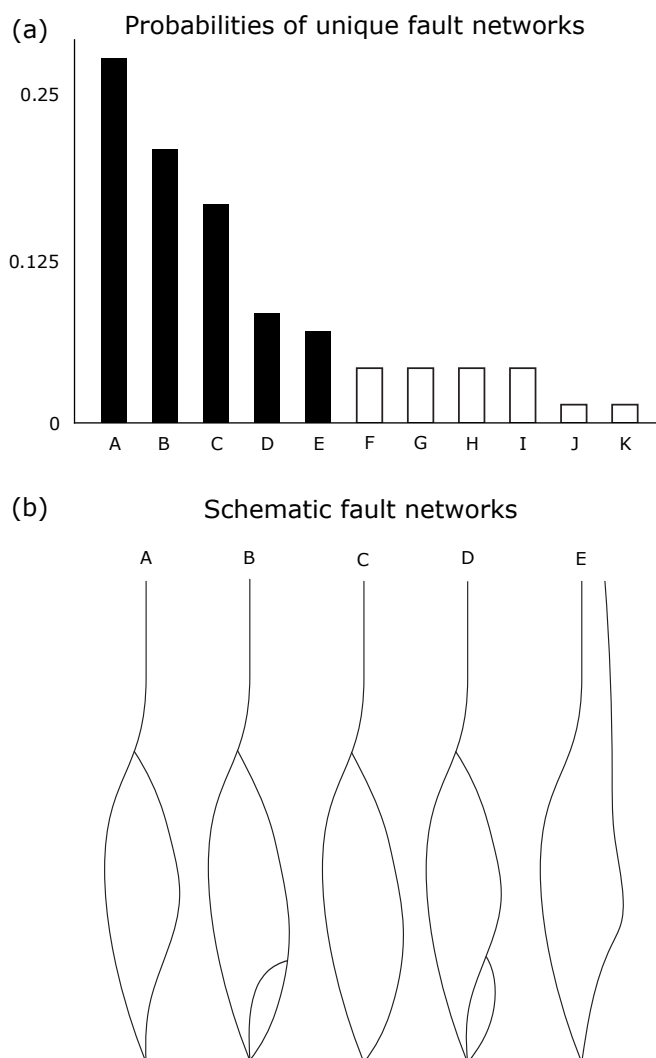
Figure 6. Probabilities of unique fault network topologies (a) with corresponding schematic fault networks (b) of the five most likely networks.

interpreting *both* F2a and F2b, and which one abuts the other. The few students who branched off the southern part of Fault 3 towards the West interpreted Fault 2b as part of Fault 3, but did not connect it to the FN of Fault 1 and 2.

3.2 Fault throw and horizon uncertainties

Results of the fault throw analysis are plotted in Fig. 7, showing median fault throw with the associated standard deviation
5 along fault strike direction. The throw profile of Fault 1 (Fig. 7a) shows a distinct sinuous shape spatially associated with its interaction with Fault 2. Fault throw uncertainty remains relatively constant along the strike (around $\pm 30\ m$), while rising
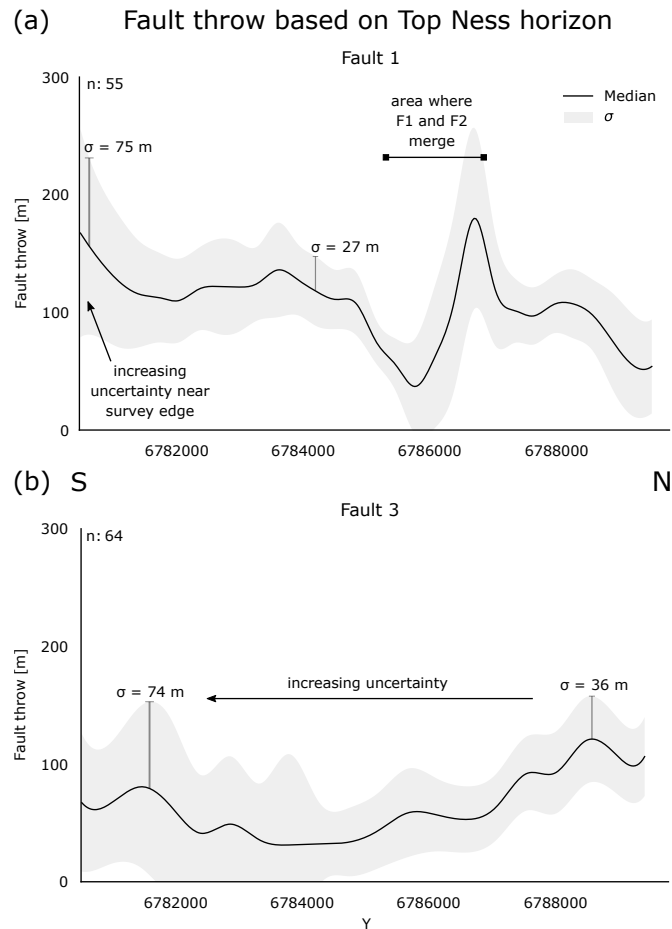
Figure 7. Results of fault throw analysis for Faults 1 (a) and 3 (b), showing the median fault throw in black, with respective standard deviation in grey.

sharply to about $\pm 75\ m$ at the southern edge of the seismic cube. The throw profile of Fault 3 (Fig. 7b) shows two distinct levels of throw uncertainty. In the northern half fault throw uncertainty remains relatively constant at around $\pm 36\ m$. This changes in the southern part of the fault, where fault throw uncertainty rises to up to $\pm 74\ m$.

Figure 8a shows the average Top Ness horizon basemap for all interpretations combined. Overall the horizon interpretations

5   are increasing in depth from SE towards the NW of the domain. Figure 8b shows the associated standard deviation of the average Ness horizon interpretation, with overlay of mean fault intersections and well locations. We observe large horizon uncertainties in vicinity to both Faults 1 and 2. Interpretation uncertainties are significantly reduced surrounding well locations in the western part of the study domain, while the effect is diminished towards the east, the reasoning of which is discussed later.
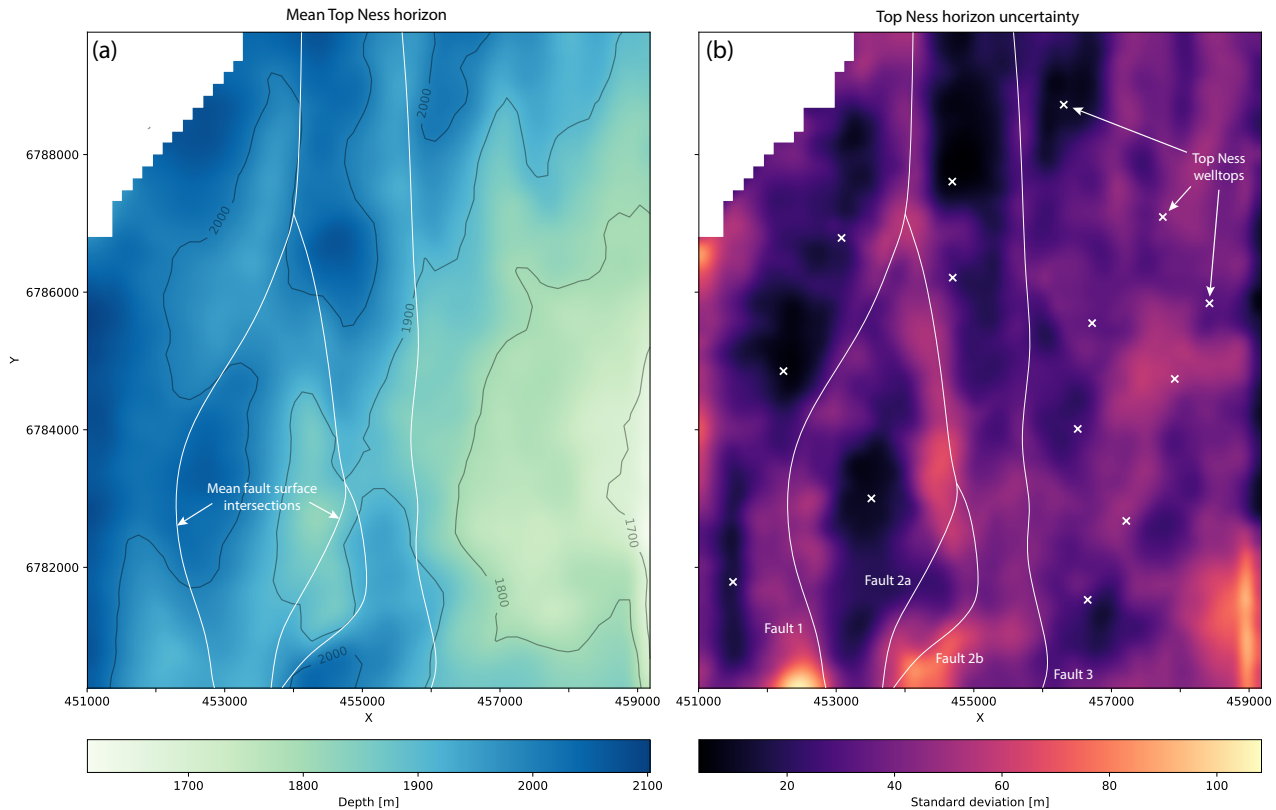
Figure 8. (a) Basemap of average Top Ness horizon from all interpretations; (b) Standard deviation of the average Top Ness horizon from all interpretations with overlaid mean fault surfaces (white lines) and welltop locations (white crosses).

3.3 Seismic data quality

To assess influences of seismic data quality on fault interpretation uncertainty we made use of the RMS Amplitude (RMSA) attribute as a proxy for reflector strength (strong horizon reflectors aiding the interpretation of faults result in high RMSA values). Specifically, we investigated the example of Fault 3, as it shows significant gradual changes in interpretation uncertainty

5   across the seismic dataset (Fig. 3c and 7b). Figure 9 shows four averaged RMSA responses with corresponding fault stick interpretation histograms (Fig. 9a-d) from the locations shown as white boxes in Fig. 9.1. In the northern extent of the seismic slice, Fault 3 is closely bounded by strong horizon reflectors, as shown in in the RMSA slice (Fig. 9.1), seismic slice (Fig. 9.2) and inline section A, focusing the students interpretations, as seen in the corresponding histogram of fault interpretations (Fig. 9a). The histogram shows a bimodal distribution, as some students interpreted the fault further towards the East, where another

10   fault is present (Fault 4, see Fig. 1b). The overall uncertainty related to the interpretation of the actual Fault 3 appears to be Gaussian, with the standard deviation roughly corresponding to the trough seen in the RMSA response. Further towards the south of the dataset, the RMSA response diminishes east of Fault 3, while remaining strong on the western side (Fig. 9b). The

10

fault interpretations show a stronger spread with thicker tails in the histogram, especially towards the West, where interpretations are then bounded by strong seismic reflectors. Further south the seismic response degrades and is noisy (Fig. 9.1 and B), which is reflected by the homogeneous RMSA values (Fig. 9c). The corresponding fault interpretations show an increase in uncertainty, appearing nearly uniformly distributed but showing some consistency in the interpretation of Fault 3 (slight crest).

5 At the southern end of the slice, RMSA responses increase again (Fig. 9d). The distribution of fault interpretations shows a bimodal distribution, as seen before in the map view 2-D histograms shown in Fig. 3. The histogram roughly resemble two very broad, overlapping Normal distributions.

4 Discussion

4.1 Key findings

10 Our work has shown that uncertainties in fault stick placement correlate with seismic reflector strengths. In areas of high data constraint this uncertainty is strongly constrained between areas of high RMSA response (Fig. 9a). Our analysis shows how interpretation uncertainty increases with a decrease in data constraints (Fig. 9b). This trend culminates in near-maximal uncertainty in areas of high seismic noise (Fig. 9c). The spread in fault stick placement appears to not be entirely driven by seismic noise, but rather appears to be, at least partly, guided by the surrounding interpretations in areas of higher data quality

15 (Fig. 9b, d), allowing interpreted faults to conform to common fault shape models (e.g. to avoid sudden shifts in fault plane orientation). In areas of low data quality the corresponding uncertainty in fault placement seems related more to conceptual uncertainties of fault network topology—e.g. interpretations of Fault 3 branching off towards the East or West (as seen in Fig. 3a, d).

While the domino structure of the study area makes overall tectonic conceptual uncertainty less significant, the low seismic

20 data quality makes it a challenging interpretation project. So despite the increased information density provided by 3-D seismic surveys, significant fault network topology uncertainties remain (Fig. 6). Our study also shows that uncertainties in the placement of faults sticks appears to increase linearly with depth (Fig. 5). This is an important finding for approximating uncertainty trends with depth, and is especially important as seismic image quality tends to decrease with depth. Additional studies on different seismic datasets could yield useful information about how these fault uncertainties might depend on seismic image

25 data quality, as seen here, and how uncertainties may be different in other tectonic and stratigraphic settings.

Our analysis of Top Ness horizon interpretation uncertainties shows the correlation of uncertainty with fault proximity (Fig. 8b). Horizon interpretations surrounding Fault 3 in the Northern part show only slight increases in uncertainty towards the fault, as they are strongly constrained by wells and high data quality (see Fig. 8b and 9A). With decreasing seismic data quality towards the South we also see an increase in uncertainty surrounding Fault 3, which also shows in the increasing fault throw

30 uncertainty seen if Fig. 7b. This trend is not evident for the throw across Fault 1, with the Top Ness horizon being better constrained on both sides, with overall higher seismic image data quality. We have also shown uncertainty in fault orientations (Fig. 4), and the inadequacy of summarizing fault orientation using a deterministic mean pole, as in Fossen and Hesthammer
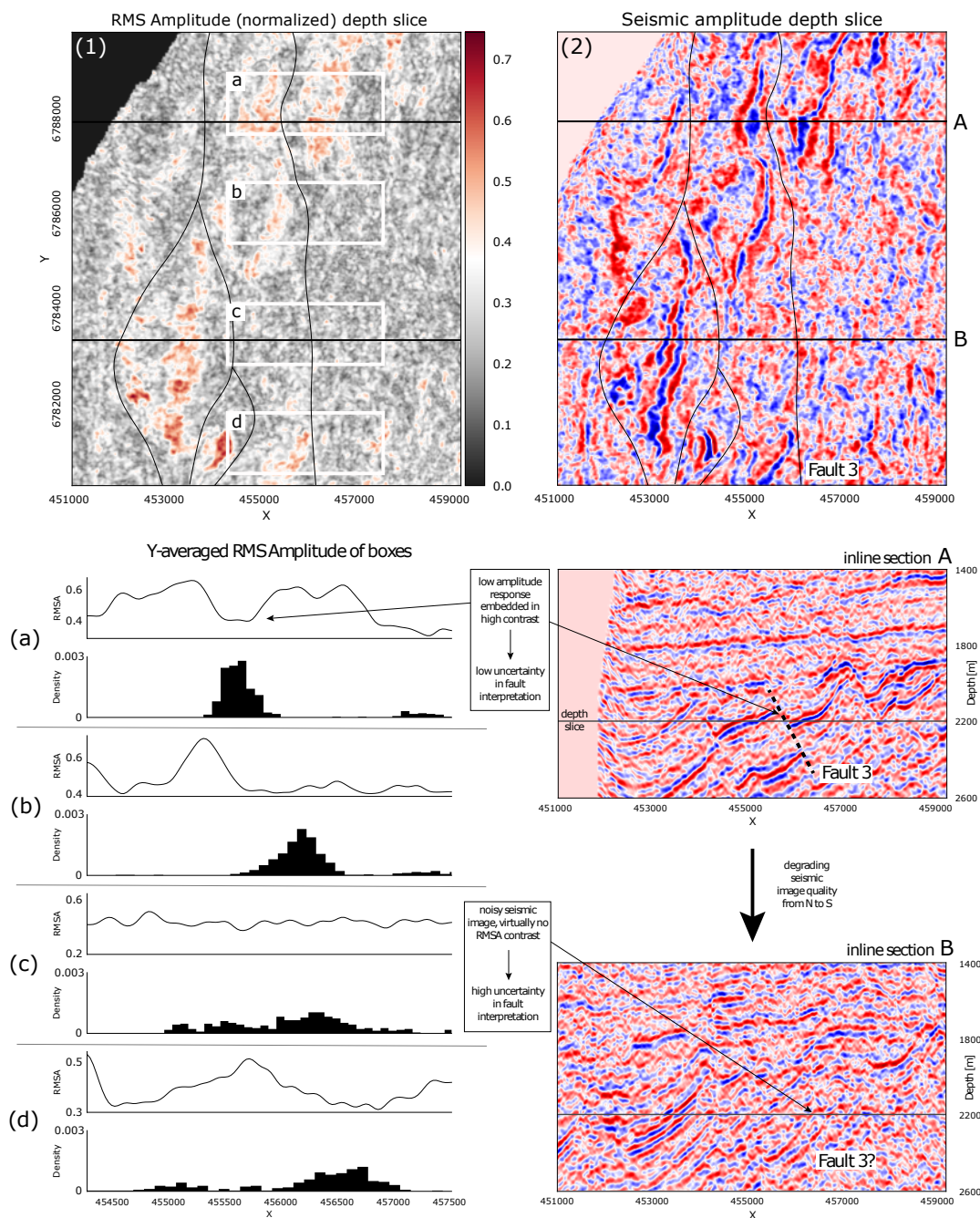
Figure 9. Depth slice of RMSA attribute (1) and seismic cube (2) with locations (black horizontal lines) of two inline sections (A, B). Four averaged RMSA responses with corresponding student Fault 3 stick interpretations are plotted in a-d, with their locations noted in the RMSA depth slice (1). The inline sections A and B correspond to the RMSA responses a and b, respectively.

(1998). This inadequacy results from sinusoidal fault map pattern (Fig. 3a) and curved 3-D geometries on-top of uncertain fault stick placements.

We also see strong decreases in uncertainty surrounding wells in the West of the study area (Fig. 8b). The trend of increasing uncertainty in horizon location from west to east could be attributed to the decrease in seismic image data quality. But we

5 would also expect for the horizon uncertainties to be reduced within the immediate surroundings of the wells. One possible explanation for this could be that students focused their interpretation efforts on the higher quality western part of the seismic cube due to the time constraints on the interpretation project.

4.2 Implications for deterministic modelling

Our results and analysis suggest that the uncertainties recorded in 2-D seismic interpretation experiments (e.g. Bond et al.,

10 2007; Bond, 2015) are similarly seen in the interpretation of 3-D seismic image data. Akin to the 2-D experiment and analysis of Alcalde et al. (2017b), we show a correlation between seismic image quality and interpretation uncertainty. We have quantified the impact of fault uncertainty on fault network topology and fault and horizon uncertainty on fault throw. The fault network topology in a 'traditional' deterministic geomodel is important as it determines the number of fault blocks and hence the degree to which stratigraphic units are separated (by faults). This information is imperative to the understanding of

15 reservoir compartmentalization in hydrocarbon reservoirs, connectivity and flow characteristics of ground water aquifers and for geothermal projects. Simply, reservoir performance can be significantly affected by fault network topology and understanding the uncertainties in fault network topology, and hence reservoir connectivity, can be critical to the planning of production strategies. The type of fault network topology information available in Fig. 6 could be used to inform reservoir modelling to guide multiple production strategies (e.g. multiple deterministic models are made) and for informed history matching during

20 field operation when reservoir models have been developed from single deterministic models and need to be updated.

Although not developed in detail in this paper, our analysis of fault throw uncertainties highlight that the use of fault throw information, e.g. to predict fault sealing properties such as shale gouge ratio (Yielding, 2002; Vrolijk et al., 2016), could be significantly affected by uncertainty in the interpretation of 3-D seismic image cubes. Our work highlights areas where uncertainties in fault throw are likely to increase: with increasing distance from wells, where seismic image quality is poor

25 (and correspondingly with increasing depth), and where faults join or abut. Modelling of uncertainties in fault throw and using information such as that derived here to inform where uncertainties are likely to be greater could provide the basis for more informed modelling of fault seal parameters, such as through stochastic modelling discussed below, or integrated as uncertainty parameters into deterministic geo- and reservoir models. In summary, fault throw uncertainty together with fault network topology uncertainty has the potential to significantly alter predicted fluid-flow patterns in the crust with implications

30 for water-resources, reactive element transfer (e.g. to inform nuclear waste disposal engineering), or hydrocarbon and energy production.

4.3 Implications for stochastic modelling

Although we can outline how uncertainty information could be used to better inform use of deterministic models and their in-
herent uncertainties, advances in both computational capabilities and implicit structural geomodelling have allowed for major
improvements in the incorporation of uncertainties into structural geomodels by means of stochastic simulations. At its core

5 stochastic structural geomodelling requires adequate disturbance distributions to obtain reasonable estimates of geomodel un-
certainty (see Wellmann and Caumon, 2018). This uncertainty parametrization can be used to better establish and account for
interpretation uncertainties on-top of deterministic modelling workflows using a hybrid approach based on a single determinis-
tic or multiple deterministic models. For example, a deterministic fault network topology model with fault throw uncertainties
parameterized, or multiple deterministic models to characterize the most probable fault network topologies (e.g. Fig. 6) with

10 fault throw uncertainties parameterized. Such hybrid approaches may provide the best solutions when the time and compu-
tational costs of full stochastic modelling are too high and/or when elements of the uncertainty in the geomodel are not best
represented as simple stochastic functions, such as different conceptual models (e.g. for fault network topologies).

The work of Pakyuz-Charrier et al. (2018) discusses the importance of proper parametrization of input data measurement
uncertainty when constructing stochastic geomodels, but little is known about the uncertainties in interpreting the dense 3-D

15 seismic datasets to obtain such input data for structural geomodels. Our work not only provides a first look at how significant
these uncertainties can be, but additionally provides a first order approximation for parametrization of fault and horizon inter-
pretation uncertainties within stochastic geomodels. Student interpretations will most certainly reside within the upper range
of interpretation uncertainty, but we argue that it provides significant value to the parametrization of the emergent Bayesian
approaches to stochastic structural geomodelling (Caers, 2011; de la Varga and Wellmann, 2016; Wellmann et al., 2017), as

20 it could provide informed—but not overly constrained—prior parametrization that can be reduced by case-specific geological
likelihood functions and auxiliary data integration. We also agree with Caers (2018) on the need for a rigorous methodology of
falsification in geomodelling. The integration of adequately parameterized seismic interpretation uncertainties into a Bayesian
geomodelling framework could enable a quality control of the interpretation by probabilistic assessment of the stochastic geo-
model against geological likelihood functions (e.g. fault length and throw relationships, fault population distributions, analog

25 studies).

Our findings underline the complexity involved in the adequate parametrization of interpretation uncertainty in stochastic
geomodelling: while Normal distributions may capture uncertainty adequately in areas of good seismic imaging (Fig. 9a),
skewed fat-tailed distributions (e.g. Cauchy; Fig. 9b) or even Uniform distributions (Fig. 9c) are reasonable choices with
degrading seismic quality. When implicitly modelling 3-D geological surfaces, many approaches are based on both surface

30 points and strike and dip information. The latter carry significantly higher amounts of information (Calcagno et al., 2008;
Laurent et al., 2016; Grose et al., 2017) than the surface points, thus emphasizing the need to quantify their uncertainty if it
is used to generate and constrain 3-D stochastic geomodels. The use of van Mises-Fisher distributions to model uncertainty
of orientation vectors was shown as a robust way to describe surface orientation uncertainty (Pakyuz-Charrier et al., 2018),

and our analysis could provide valuable information for their parametrization in areas of high interpretation uncertainty within sedimentary basins.

4.4 Implications for machine learning

Recent efforts in automating seismic interpretation through the use of, mainly, Neural Networks (NN) has been increasingly
5 successful in interpreting high quality (synthetic) seismic data (e.g. Huang et al., 2017; Dramsch and Lüthje, 2018; Wu et al., 2018). But NNs inherently do not take into account any geological reasoning skills that could make sense of areas of low seismic image data quality, but rather infer abstract features from their training data. And while NNs can be constructed and trained probabilistically, and thus enable uncertainty quantification of their outputs, they are likely to require additional information about the structures to be interpreted in areas where interpretation suffers from low data quality. In our analysis of
10 the uncertainties in interpretations of the Gullfaks field 3-D seismic cube the interpretations of faults in areas of low seismic image quality conform to known fault geometries and topologies and are likely informed by interpretations of adjacent higher quality seismic image data, rather than their uncertainty distributions being simply correlated to seismic image quality (Fig. 9). Such evidence highlights the nuances in geological interpretation, and the difficulties in creating algorithms that represent the complexities of human thought processes. Irrespective of how easy it is, or otherwise, to apply our findings to inform
15 automated interpretation efforts, there is value in studies such as the one presented here in generating understanding as to when and where such machine learning processes maybe applied effectively and how they could be improved by integrating geological knowledge, maybe in the form of *logic rules* that influence NN weights and biases (Hu et al., 2016). Lu et al. (2018) show the use of Generative Adversarial Networks (GANs) in improving fault interpretation of low-resolution seismic image data by generating supersampled high-quality seismic images from lower quality data. One possibility could be to train similar
20 NNs on the structural geology represented by ideal synthetic seismic image data and artificially noisy perturbations of the same to let NNs learn how ideal structures that underlie noisy seismic image data might look like. They could then possibly generate possible higher-quality realizations of noisy, uncertain areas of seismic images to support interpretation efforts. Overall, the complex interplay of the underlying geology, computational and conceptual challenges of the machine learning approaches and the human-induced uncertainties will require strongly interdisciplinary approaches to combine state-of-the-art algorithms
25 and geological domain knowledge to further automate the laborious and uncertain task of 3-D seismic interpretation.

References

Alcalde, J., Bond, C. E., Johnson, G., Butler, R. W., Cooper, M. A., and Ellis, J. F.: The Importance of Structural Model Availability on Seismic Interpretation, Journal of Structural Geology, 97, 161–171, https://doi.org/10.1016/j.jsg.2017.03.003, 2017a.

Alcalde, J., Bond, C. E., Johnson, G., Ellis, J. F., and Butler, R. W.: Impact of Seismic Image Quality on Fault Interpretation Uncertainty, GSA Today, https://doi.org/10.1130/GSATG282A.1, 2017b.

Alcalde, J., Bond, C. E., and Randle, C. H.: Framing Bias: The Effect of Figure Presentation on Seismic Interpretation, Interpretation, 5, T591–T605, 2017c.

Biondi, B.: 3D Seismic Imaging, Investigations in Geophysics, Society of Exploration Geophysicists, https://doi.org/10.1190/1.9781560801689, 2006.

Bond, C., Gibbs, A., Shipton, Z., and Jones, S.: What Do You Think This Is? "Conceptual Uncertainty" in Geoscience Interpretation, GSA Today, 17, 4, https://doi.org/10.1130/GSAT01711A.1, 2007.

Bond, C. E.: Uncertainty in Structural Interpretation: Lessons to Be Learnt, Journal of Structural Geology, 74, 185–200, https://doi.org/10.1016/j.jsg.2015.03.003, 2015.

Bond, C. E., Philo, C., and Shipton, Z. K.: When There Isn't a Right Answer: Interpretation and Reasoning, Key Skills for Twenty-First Century Geoscience, International Journal of Science Education, 33, 629–652, https://doi.org/10.1080/09500691003660364, 2011.

Caers, J.: Modeling Uncertainty in the Earth Sciences: Caers/Modeling Uncertainty in the Earth Sciences, John Wiley & Sons, Ltd, Chichester, UK, https://doi.org/10.1002/9781119995920, 2011.

Caers, J.: Bayesianism in the Geosciences, in: Handbook of Mathematical Geosciences: Fifty Years of IAMG, edited by Daya Sagar, B., Cheng, Q., and Agterberg, F., pp. 527–566, Springer International Publishing, Cham, https://doi.org/10.1007/978-3-319-78999-6_27, 2018.

Calcagno, P., Chilès, J. P., Courrioux, G., and Guillen, A.: Geological Modelling from Field Data and Geological Knowledge: Part I. Modelling Method Coupling 3D Potential-Field Interpolation and Geological Rules, Physics of the Earth and Planetary Interiors, 171, 147–157, https://doi.org/10.1016/j.pepi.2008.06.013, 2008.

de la Varga, M. and Wellmann, J. F.: Structural Geologic Modeling as an Inference Problem: A Bayesian Perspective, Interpretation, 4, SM1–SM16, https://doi.org/10.1190/INT-2015-0188.1, 2016.

Dramsch, J. and Lüthje, M.: Deep-Learning Seismic Facies on State-of-the-Art CNN Architectures, in: SEG Technical Program Expanded Abstracts 2018, SEG Technical Program Expanded Abstracts, pp. 2036–2040, Society of Exploration Geophysicists, https://doi.org/10.1190/segam2018-2996783.1, 2018.

Fossen, H. and Hesthammer, J.: Structural Geology of the Gullfaks Field, Northern North Sea, Geological Society, London, Special Publications, 127, 231–261, https://doi.org/10.1144/GSL.SP.1998.127.01.16, 1998.

Freeman, B., Yielding, G., and Badley, M.: Fault Correlation during Seismic Interpretation, First Break, 8, 1990.

Frodeman, R.: Geological Reasoning: Geology as an Interpretive and Historical Science, Geological Society of America Bulletin, 107, 960–0968, https://doi.org/10.1130/0016-7606(1995)107<0960:GRGAAI>2.3.CO;2, 1995.

Grose, L., Laurent, G., Aillères, L., Armit, R., Jessell, M., and Caumon, G.: Structural Data Constraints for Implicit Modeling of Folds, Journal of Structural Geology, 104, 80–92, https://doi.org/10.1016/j.jsg.2017.09.013, 2017.

Hesthammer, J. and Fossen, H.: Seismic Attribute Analysis in Structural Interpretation of the Gullfaks Field, Northern North Sea | Petroleum Geoscience, Petroleum Geoscience, 3, 13–26, 1997.

Hu, Z., Ma, X., Liu, Z., Hovy, E., and Xing, E.: Harnessing Deep Neural Networks with Logic Rules, arXiv:1603.06318 [cs, stat], 2016.

Huang, L., Dong, X., and Clee, T. E.: A Scalable Deep Learning Platform for Identifying Geologic Features from Seismic Attributes, The Leading Edge, 36, 249–256, https://doi.org/10.1190/tle36030249.1, 2017.

Jones, E., Oliphant, T., Peterson, P., et al.: SciPy: Open Source Scientific Tools for Python, 2001.

5 Laurent, G., Ailleres, L., Grose, L., Caumon, G., Jessell, M., and Armit, R.: Implicit Modeling of Folds and Overprinting Deformation, Earth and Planetary Science Letters, 456, 26–38, https://doi.org/10.1016/j.epsl.2016.09.040, 2016.

Lu, P., Morris, M., Brazell, S., Comiskey, C., and Xiao, Y.: Using Generative Adversarial Networks to Improve Deep-Learning Fault Interpretation Networks, The Leading Edge, 37, 578–583, https://doi.org/10.1190/tle37080578.1, 2018.

Macrae, E. J.: Uncertainty in Geoscience Interpretation: Statistical Quantification of the Factors That Affect Interpretational Ability and 10 Their Application to the Oil and Gas Industry, p. 264, 2013.

Macrae, E. J., Bond, C. E., Shipton, Z. K., and Lunn, R. J.: Increasing the Quality of Seismic Interpretation, Interpretation, 4, T395–T402, https://doi.org/10.1190/INT-2015-0218.1, 2016.

McKinney, W.: Pandas: A Foundational Python Library for Data Analysis and Statistics, Python for High Performance and Scientific Computing, pp. 1–9, 2011.

15 Oliphant, T. E.: A Guide to NumPy, vol. 1, Trelgol Publishing USA, 2006.

Pakyuz-Charrier, E., Lindsay, M., Ogarko, V., Giraud, J., and Jessell, M.: Monte Carlo Simulation for Uncertainty Estimation on Structural Data in Implicit 3-D Geological Modeling, a Guide for Disturbance Distribution Selection and Parameterization, Solid Earth, 9, 385–402, https://doi.org/https://doi.org/10.5194/se-9-385-2018, 2018.

Vrolijk, P. J., Urai, J. L., and Kettermann, M.: Clay Smear: Review of Mechanisms and Applications, Journal of Structural Geology, 86, 20 95–152, https://doi.org/10.1016/j.jsg.2015.09.006, 2016.

Wellmann, J. F. and Caumon, G.: 3-D Structural Geological Models: Concepts, Methods, and Uncertainties, in: Advances in Geophysics, vol. 59, 1st edn., 2018.

Wellmann, J. F., de la Varga, M., Murdie, R. E., Gessner, K., and Jessell, M.: Uncertainty Estimation for a Geological Model of the Sandstone Greenstone Belt, Western Australia – Insights from Integrated Geological and Geophysical Inversion in a Bayesian Inference Framework, 25 Geological Society, London, Special Publications, p. SP453.12, https://doi.org/10.1144/SP453.12, 2017.

Wu, X., Shi, Y., Fomel, S., and Liang, L.: Convolutional Neural Networks for Fault Interpretation in Seismic Images, in: SEG Technical Program Expanded Abstracts 2018, SEG Technical Program Expanded Abstracts, pp. 1946–1950, Society of Exploration Geophysicists, https://doi.org/10.1190/segam2018-2995341.1, 2018.

Yielding, G.: Shale Gouge Ratio — Calibration by Geohistory, in: Norwegian Petroleum Society Special Publications, edited by Koestler, 30 A. G. and Hunsdale, R., vol. 11 of *Hydrocarbon Seal Quantification*, pp. 1–15, Elsevier, https://doi.org/10.1016/S0928-8937(02)80003-0, 2002.